

Chapter 4: Nanoscale optics: inter-particle forces

Luciana C. Dávila Romero and David L. Andrews

1 Introduction

The nature and variety of optical forces that operate on particles of atomic, molecular, nano- or micro- scale dimensions are in principle similar to those that relate to the effect of light on larger particles. When compared to the latter, however, a significant difference in practical terms is the greater ease, in the case of microparticles, in overcoming gravity. This feature facilitates the study of suspensions or surface layers, for example, in systems comprising micron or nanometer sized particles. The distinct advantage of the nanoscale, in this respect, is nonetheless offset against much more influential levels of thermal motion. The latter problem, particularly acute in the case of atomic samples, is commonly overcome by the use of cold atom traps and optical molasses instrumentation – utilizing atomic cooling through momentum exchange with absorbed and emitted photons. In any such context, conventional optical tweezers and Maxwell-Bartoli mechanisms represent the operation of optomechanical forces whose origins are well understood, and which characteristically operate on individual particles of matter. Further distinctions in behavior can then be drawn on the basis of material composition, the salient response functions being cast in terms that reflect atomic, molecular, dielectric or metallic constitution, for example. In the last of these, the distinctively complex refractive index represents a quality admitting further opportunities to tailor dispersive optical forces, often supplemented by an exploitation of plasmonic effects.

A relatively recent flurry of activity has been prompted by the discovery and verification of something quite different: an optomechanical force that operates *between* particles at nanoscale separations. The first theoretical proof that intense laser light can produce an optically modified potential energy surface for particle interactions was provided by Thirunamachandran almost thirty years ago [1] – but the laser intensities that appeared necessary then represented a significant deterrent. However, before the end of the decade a landmark paper by Burns *et al.* [2] verified the effect experimentally. This latter work also provided the first graphs, for the simplest case of two identical, spherical particles, of energy

against separation – graphs exhibiting striking landscapes of rolling potential energy maxima and minima, as illustrated in Fig. 1. Recognition of the enormous potential for practical applications quickly came about, the prospects being almost immediately flagged in an influential futurology of chemistry [3]. Subsequent studies have shown that optically induced inter-particle forces offer a number of highly distinctive features which can be exploited for the controlled optical manipulation of matter. The terms ‘optical binding’ and ‘optical matter’, which have gained some currency for such forces, highlight the possibilities for a significant interplay with other interactions, such as chemical bonding and dispersion forces. Exploiting such interactions, new opportunities for creating optically ordered matter have already been demonstrated both theoretically and experimentally [4-11].

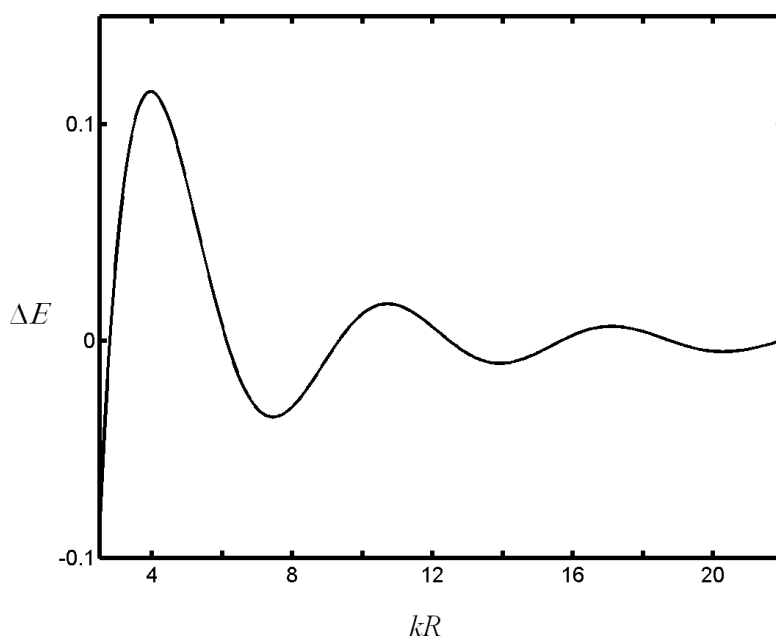


Figure 1: Dependence of optically-induced potential energy, for a pair of particles separated by distance R , plotted against kR , where $k = 2\pi/\lambda$ and λ is the laser wavelength. The inter-particle axis is aligned with the electric field of the radiation; the locations of the energetically stable minima depend on dispersion properties (see later). Graphs of similar form, for example in refs [2, 8], provide a compelling motif for the subject.

At this juncture, progress in theory is developing along several fronts, with many studies invoking essentially classical descriptions of the radiation field. Some of the most adventurous relate to perhaps the most demanding experimental challenge – the possibility of engaging off-resonant laser light with Bose-Einstein condensates to achieve ‘superchemistry’, i.e. the coherent manipulation and assembly of atoms and molecules [12, 13]. In several

treatments, paraxial wave equations have been adopted to describe optical binding between micron-sized spherical particles, in the presence of counterpropagating beams [14-15], the results here being analyzed in terms of the relative refractive indices of the spheres and the surrounding medium. Such studies are valid in the Mie size regime, *i.e.* where the sphere diameter exceeds the wavelength, and input fields are well approximated as paraxial. Considering particles of like dimensions, Chaumet and Nieto-Vesperinas [8] have derived results both for isolated spheres, and for spheres near a surface. In the isolated case they have found that inter-particle forces depend significantly on the polarization and wavelength of the incident light, and the particle size. Furthermore, Ng and Chan [16] have determined the equilibrium positions in an array of evenly spaced particles, aligned in parallel with the wave-vector of the optical input. Extending the range of applications, studies of optical trapping and binding of cylindrical particles have been carried out by Grzegorzczuk *et al.* [17-18].

Further opportunities for application, and other readily achievable areas of relevance, are now being identified with the benefit of a comprehensive theory based on QED – quantum electrodynamics [19,20]. Based on this theory, calculations on carbon nanotubes, for example, have already the indicated dependences on particle orientation, suggesting possibilities for optically modifying the morphology of deposited nanotube films [21], while applications to other dielectric nanoparticles in optical vortex fields have identified opportunities for new forms of optical patterning and clustering [22]. Some of the most recent work has established other, more exotic effects, such as an optically induced shift in the equilibrium bond length of van der Waals dimers (molecular pairs held together by weak hydrogen bonds) and, in molecular solids, bulk optomechanical deformation [23]. In the following, Section 2, we first rehearse and explain the state of the art QED theory, placing the various representations within a single, consistent framework. With reference to the key equations and against this background, Section 3 provides a concise overview of the applications, and the chapter concludes with a look to the future in the Discussion, Section 4.

2 QED description of optically induced pair forces

In the perturbative derivation of optically induced pair forces, as with more common inter-particle coupling forces, calculations are generally performed on a system in which each particle resides in its lowest-energy, stable state. For the development of a QED theory, the system state has to be more precisely specified – as one in which both particles and the radiation field are in the ground state. This system state couples with other short-lived states in which the electromagnetic field has a non-zero occupation number for one or more radiation modes. The *dispersion interaction*, traditionally interpreted as a coupling between mutually induced moments, emerges from a fourth-order perturbative calculation based on the exchange of two virtual photons, each created at one particle and annihilated at the other. The two virtual quanta may (but need not) overlap in time as they propagate between the two units. Cast in such terms, the theory delivers a result – the Casimir-Polder formula – valid for all distances, correctly accounting for the retardation features which lead to a long-range R^{-7} asymptote dependence on the pair separation R [24-30]. The virtual photon interpretation also lends a fresh perspective to the physics involved in the more familiar R^{-6} range dependence known as the van der Waals interaction – the attractive part of the Lennard-Jones potential, which operates at shorter distances and which is largely responsible for the cohesion of condensed phase matter [31].

The photonic basis for the dispersion interaction strongly suggests that other effects may be manifest when intense light is present, i.e. when calculations are performed on a basis state for which the occupation number of at least one photon mode is non-zero. Indeed it is the same, fourth order of perturbation theory that gives the leading result; the annihilation and creation of one photon from the occupied radiation mode in principle substitute for the paired creation and annihilation events of one of the two virtual photons involved in the Casimir-Polder calculation. It is clear that the result of any such calculation on optically conferred pair energies will exhibit a linear dependence on the photon number of the occupied mode. Cast in terms of experimental quantities, this will be manifest as an energy shift ΔE_{ind} with a corresponding proportionality to the irradiance of throughput radiation. The corresponding laser-induced coupling forces can be determined from the potential energy result, as the spatial derivative.

2.1 Quantum foundations

To begin, consider the coupling between two particles, with no assumed symmetry, whose laser-induced interactions involve the absorption of a real input photon at one particle and the stimulated emission of a real photon at the other one, with a virtual photon acting as a messenger between the two. The throughput radiation suffers no overall change in its state. Following the Power-Zienau–Woolley approach [32-35], writing the interactions of the vacuum electromagnetic fields with particle ξ in the electric–dipole approximation, we have the interaction Hamiltonian;

$$H_{\text{int}}^{\xi} = -\varepsilon_o^{-1} \sum_{\xi} \boldsymbol{\mu}(\xi) \cdot \mathbf{d}^{\perp}(\mathbf{R}_{\xi}), \quad (2.1)$$

where $\boldsymbol{\mu}(\xi)$ and \mathbf{R}_{ξ} respectively denote the electric-dipole moment operator and the position vector of dielectric nanoparticles labeled ξ . The operator $\mathbf{d}^{\perp}(\mathbf{R}_{\xi})$ represents the transverse electric displacement field, expressible in the following general mode-expansion;

$$\mathbf{d}^{\perp}(\mathbf{R}_{\xi}) = i \sum_{\mathbf{k}, \lambda} \left(\frac{\hbar c k \varepsilon_o}{2V} \right)^{1/2} \left[\mathbf{e}^{(\lambda)}(\mathbf{k}) a^{(\lambda)}(\mathbf{k}) \exp(i\mathbf{k}\mathbf{R}_{\xi}) - \bar{\mathbf{e}}^{(\lambda)}(\mathbf{k}) a^{\dagger(\lambda)}(\mathbf{k}) \exp(-i\mathbf{k}\mathbf{R}_{\xi}) \right]. \quad (2.2)$$

In equation (2.2), V is the quantization volume, and summation is taken over modes indexed by wave-vector \mathbf{k} and polarization λ ; a and a^{\dagger} are annihilation and creation operators, respectively, and \mathbf{e} represents the electric field unit vector, with $\bar{\mathbf{e}}$ being its complex conjugate. For present purposes the distinction between \mathbf{e} and $\bar{\mathbf{e}}$ can be dropped on the assumption that only plane polarizations are to be entertained – which is consistent with experimental practice. Since the laser-induced coupling involves four matter–photon interactions, it requires the application of fourth–order perturbation theory (within the electric dipole approximation) and the energy is explicitly given by;

$$\Delta E_{\text{ind}} = \text{Re} \left[\sum_{t,s,r} \frac{\langle i | H_{\text{int}} | t \rangle \langle t | H_{\text{int}} | s \rangle \langle s | H_{\text{int}} | r \rangle \langle r | H_{\text{int}} | i \rangle}{(E_i - E_t)(E_i - E_s)(E_i - E_r)} \right], \quad (2.3)$$

In general, an arbitrary ket $|\varepsilon\rangle$ here refers to a member of the set of basis states of the unperturbed Hamiltonian, such that we have;

$$|s\rangle = |\text{mol}\rangle_s \otimes |\text{rad}\rangle_s = |\text{mol}_s; \text{rad}_s\rangle, \quad (2.4)$$

where $|\text{mol}\rangle_s$ and $|\text{rad}\rangle_s$ respectively define the status of all particles and radiation states involved. Specifically, $|i\rangle$ is the unperturbed system state and the kets $|r\rangle$, $|t\rangle$, $|s\rangle$ are virtual states.

From equations (2.1) and (2.2) it follows that each Dirac bracket in the numerator of (2.3) is associated with the creation or annihilation of a photon. Details emerge on application to a specific system; here we consider two chemically identical particles A and B , the latter displaced from A by a vector \mathbf{R} . Assuming neither particle possesses a permanent electric dipole moment, it is readily shown that each must suffer two dipole transitions, and that 48 different cases arise – each of which generates a dynamic contribution to the energy shift. As a calculational aid, these contributions are typically represented in the form of non-relativistic Feynman diagrams, as illustrated in Fig. 2. In the complete set, 24 entail absorption of the laser photon at A , and in the other 24 the same process occurs at B . The latter may be deduced on the basis of mirroring the former, in the sense that A exchanges with B , and \mathbf{R} changes sign. Accordingly we denote as $\Delta E_{ind}^{A \rightarrow B}$ the energy shift resulting from orderings in which the absorption of laser light occurs at A , and stimulated emission at B , with $\Delta E_{ind}^{B \rightarrow A}$ denoting the converse. [Note; the direction indicated by the superscript does *not* determine the direction of virtual photon propagation; amongst the contributions to $\Delta E_{ind}^{A \rightarrow B}$, for example, half involve virtual photon propagation towards B – but the other half, towards A .]

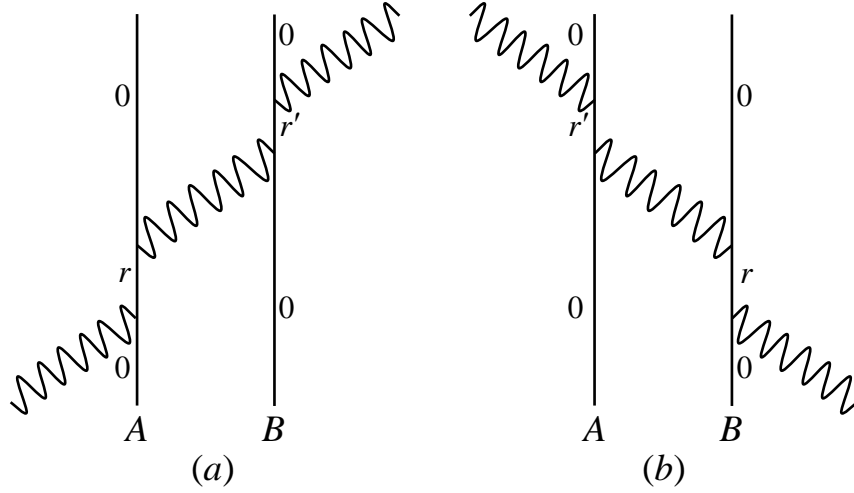


Figure 2: Two typical Feynman diagrams (each with 23 further permutations) for calculation of dynamic contributions to the laser-induced interaction energy. The verticals denote world-lines of the two particles; wavy lines outside them denote real (laser) photons and those inside, virtual photons; time progresses upwards. Adapted from [19]

Hence we have the following expression for the total induced energy shift, ΔE_{ind} ;

$$\begin{aligned}
 \Delta E_{ind} &= \Delta E_{ind}^{A \rightarrow B} + \Delta E_{ind}^{B \rightarrow A} = \Delta E_{ind}^{A \rightarrow B}(\mathbf{R}) + \Delta E_{ind}^{A \rightarrow B}(-\mathbf{R}) \\
 &= \Delta E_{ind}^{A \rightarrow B}(\mathbf{R})|_{even} + \Delta E_{ind}^{A \rightarrow B}(\mathbf{R})|_{odd} + \Delta E_{ind}^{A \rightarrow B}(\mathbf{R})|_{even} - \Delta E_{ind}^{A \rightarrow B}(\mathbf{R})|_{odd} \\
 &= 2\Delta E_{ind}^{A \rightarrow B}(\mathbf{R})|_{even}, \tag{2.5}
 \end{aligned}$$

where *even* and *odd* denote the corresponding parts of the function $\Delta E_{ind}^{A \rightarrow B}(\mathbf{R})$ with respect to \mathbf{R} . Using expression (2.3) – and after a sequence of calculational steps detailed elsewhere [19], the induced energy shift $\Delta E_{ind}^{A \rightarrow B}$ emerges as follows, using the convention of implied summation over repeated subscript (Cartesian) indices;

$$\Delta E_{ind}^{A \rightarrow B}(k, \mathbf{R}) = \left(\frac{n\hbar ck}{\epsilon_o V} \right) \text{Re} \left[e_i^{(\lambda)} \alpha_{ij}^A(k) V_{jk}^{\pm}(k, \mathbf{R}) \alpha_{kl}^B(k) e_l^{(\lambda)} \exp(-i\mathbf{k} \cdot \mathbf{R}) \right]. \tag{2.6}$$

Here n is the number of laser photons within a quantization volume V , and we have introduced the well-known dynamic polarizability tensor α_{ij}^{ξ} and the fully retarded resonance dipole-dipole interaction tensor of the general form;

$$V_{jk}^{\pm}(k, \mathbf{R}) = \frac{\exp[\mp ikR]}{4\pi\epsilon_0 R^3} \left\{ (1 \pm ikR) (\delta_{jk} - 3\hat{R}_j \hat{R}_k) - (kR)^2 (\delta_{jk} - \hat{R}_j \hat{R}_k) \right\}. \quad (2.7)$$

Given that the analytically arbitrary choice of sign has no physical consequence [36] we shall stick with the negative sign (as generally assumed without comment in older work) and drop it from our notation henceforth, i.e. $V_{jk}^{-}(k, \mathbf{R}) \equiv V_{jk}(k, \mathbf{R})$.

2.2 Defining the geometry

As a convenient starting point for an exploration, later in this Section, of various geometries and degrees of rotational freedom, we begin by considering the coupling of two fixed particles, with no assumed symmetry. The geometry for the pair is specified as follows, particle A is at the origin ($\mathbf{R}_A = \mathbf{0}$) and B is on the z axis ($\mathbf{R}_B = R\hat{\mathbf{z}}$) such that the separation between the two particles is given by $\mathbf{R} \equiv \mathbf{R}_B - \mathbf{R}_A = R\hat{\mathbf{z}}$; the angles ϕ and θ denote the orientations of the optical polarization vector respect to \mathbf{R} – see Fig. 3. The figure depicts a case where both particles have the same orientation; however, in a more general case, this will not necessarily apply.

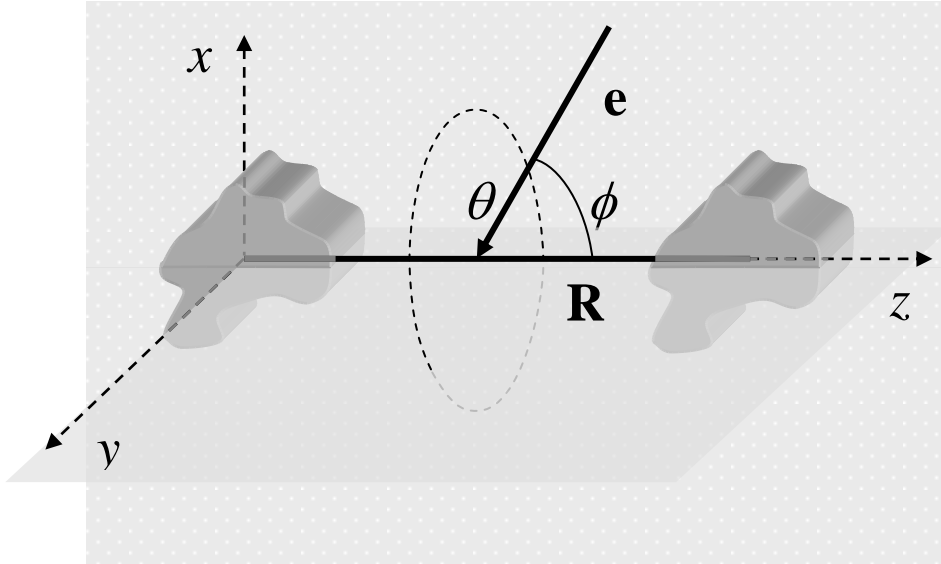


Figure 3: Geometry of the particle pair and the polarization vector \mathbf{e} of the electromagnetic field. For simplicity both particles are shown with the same orientation. In the electric-dipole approximation the direction of the optical propagation vector, is irrelevant, serving only as a constraint on possible directions of \mathbf{e} .

In order to fully describe the system with due regard to its internal degrees of freedom it is necessary to consider three frames of reference:

- a) A *fixed* frame (or *laboratory* frame), denoted by $(\hat{x}, \hat{y}, \hat{z})$ as seen in Fig. 3;
- b) For each particle, $\xi = A$ and B , a *particle* frame, chosen with regard to the particle symmetry such that the corresponding polarizability tensor is diagonalized in three non-zero components $(\hat{x}'^\xi, \hat{y}'^\xi, \hat{z}'^\xi)$.

The latter frames enter the calculations at a later stage; for the present we can refer all vectors and tensors to the fixed frame. Thus, for example, from equation (2.7) the components of the tensor $V_{jk}(k, \mathbf{R})$ are explicitly;

$$V_{jk}(k, \mathbf{R}) = \begin{cases} \frac{\exp[ikR]}{4\pi\epsilon_0 R^3} \left\{ (1-ikR) - (kR)^2 \right\} & \text{for } (jk) = \{xx, yy\}, \\ -\frac{\exp[ikR]}{2\pi\epsilon_0 R^3} (1-ikR) & \text{for } (jk) = \{zz\}, \\ 0 & \text{otherwise.} \end{cases} \quad (2.8)$$

From equations (2.6) and (2.8), and using the relationship $I = n\hbar c^2 k/V$ for the laser irradiance I , we have;

$$\Delta E_{ind}^{A \rightarrow B}(k, \mathbf{R}) = \left(\frac{I}{4\pi\epsilon_0^2 c} \right) \text{Re} \left[\left[e_i^{(\lambda)} \mathbf{Z}_{il}^{(1)} e_l^{(\lambda)} (1-ikR) - e_i^{(\lambda)} \mathbf{Z}_{il}^{(2)} e_l^{(\lambda)} (kR)^2 \right] \frac{\exp(ikR) \exp(-i\mathbf{k} \cdot \mathbf{R})}{R^3} \right], \quad (2.9)$$

where we have introduced two pair response tensors, $\mathbf{Z}_{il}^{(1)}$ and $\mathbf{Z}_{il}^{(2)}$. The latter are defined, in the pair-fixed frame, as;

$$\begin{aligned} \mathbf{Z}_{il}^{(1)} &= \mathbf{Z}_{il}^{(2)} - 2\alpha_{iz}^A \alpha_{zl}^B, \\ \mathbf{Z}_{il}^{(2)} &= \alpha_{ix}^A \alpha_{xl}^B + \alpha_{iy}^A \alpha_{yl}^B. \end{aligned} \quad (2.10)$$

When the real part of the square bracket is taken in expression (2.9) the induced energy shift is expressible as;

$$\begin{aligned} \Delta E_{ind}^{A \rightarrow B}(k, \mathbf{R}) = & \left(\frac{I}{4\pi\epsilon_o^2 c R^3} \right) \times \\ & \left\{ e_i^{(\lambda)} \mathbf{Z}_{il}^{(2)} e_l^{(\lambda)} \left[\cos(kR - \mathbf{k} \cdot \mathbf{R}) + kR \sin(kR - \mathbf{k} \cdot \mathbf{R}) - (kR)^2 \cos(kR - \mathbf{k} \cdot \mathbf{R}) \right] \right. \\ & \left. - 2e_i^{(\lambda)} \alpha_{iz}^A \alpha_{zl}^B e_l^{(\lambda)} \left[\cos(kR - \mathbf{k} \cdot \mathbf{R}) + kR \sin(kR - \mathbf{k} \cdot \mathbf{R}) \right] \right\}. \end{aligned} \quad (2.11)$$

Securing the complete result, using expression (2.5), it is apparent that the induced energy shift is given by;

$$\begin{aligned} \Delta E_{ind}(k, \mathbf{R}) = & \left(\frac{I}{2\pi\epsilon_o^2 c R^3} \right) \left\{ \left[e_i^{(\lambda)} \mathbf{Z}_{il}^{(2)} e_l^{(\lambda)} - 2e_i^{(\lambda)} \alpha_{iz}^A \alpha_{zl}^B e_l^{(\lambda)} \right] \left[\cos(kR) + kR \sin(kR) \right] \right. \\ & \left. - e_i^{(\lambda)} \mathbf{Z}_{il}^{(2)} e_l^{(\lambda)} k^2 R^2 \cos(kR) \right\} \cos(\mathbf{k} \cdot \mathbf{R}) \end{aligned} \quad (2.12)$$

The inter-particle force can be found by simply taking the derivative of the energy shift with respect to the separation of the particles;

$$\begin{aligned} \mathbf{F}_{ind} = & - \frac{\partial \Delta E_{ind}}{\partial \mathbf{R}} \\ = & \left(\frac{I}{2\pi\epsilon_o^2 c R^4} \right) \left\{ \left[e_i^{(\lambda)} \mathbf{Z}_{il}^{(2)} e_l^{(\lambda)} - 2e_i^{(\lambda)} \alpha_{iz}^A \alpha_{zl}^B e_l^{(\lambda)} \right] \times \right. \\ & \left\{ \left[3 \cos(kR) + 3kR \sin(kR) - k^2 R^2 \cos(kR) \right] \cos(\mathbf{k} \cdot \mathbf{R}) + \left[k_z R \cos(kR) + k_z k R^2 \sin(kR) \right] \sin(\mathbf{k} \cdot \mathbf{R}) \right\} \\ & \left. - e_i^{(\lambda)} \mathbf{Z}_{il}^{(2)} e_l^{(\lambda)} \left\{ \left[k^2 R^2 \cos(kR) + k^3 R^3 \sin(kR) \right] \cos(\mathbf{k} \cdot \mathbf{R}) + k_z k^2 R^3 \cos(kR) \sin(\mathbf{k} \cdot \mathbf{R}) \right\} \right\} \end{aligned} \quad (2.13)$$

We now analyze particular cases, deriving explicit results for other systems of physical interest. Particles of cylindrical symmetry are assumed, accommodating the more usual case of spherical symmetry, but also delivering results that have validity for nanotubes and most other significantly anisotropic nanoparticles.

2.3 Tumbling cylindrical pair

First we address a system in which the two particles freely rotate in the incident light as a binary system, each particle maintaining a fixed distance and orientation with respect to its counterpart. In this case we not only have the angles that define the direction of the polarization vector respect to the pair, as introduced in Fig. 3; it is also necessary to introduce three angles which will determine the relative orientations of the two components. As shown in Fig. 4, these internal angles are defined as $(\gamma_A, \gamma_B, \psi)$; γ_A is the angle between the particle A and the z axis (assuming that the \hat{z}'^A lies on the xz -plane); γ_B is the angle between the z -axis and the molecular principal axis z'^B (which may or may not lie on the xz -plane); while angle ψ is the angle between \hat{z}'^A and z'^B axes projected on to the xy -plane

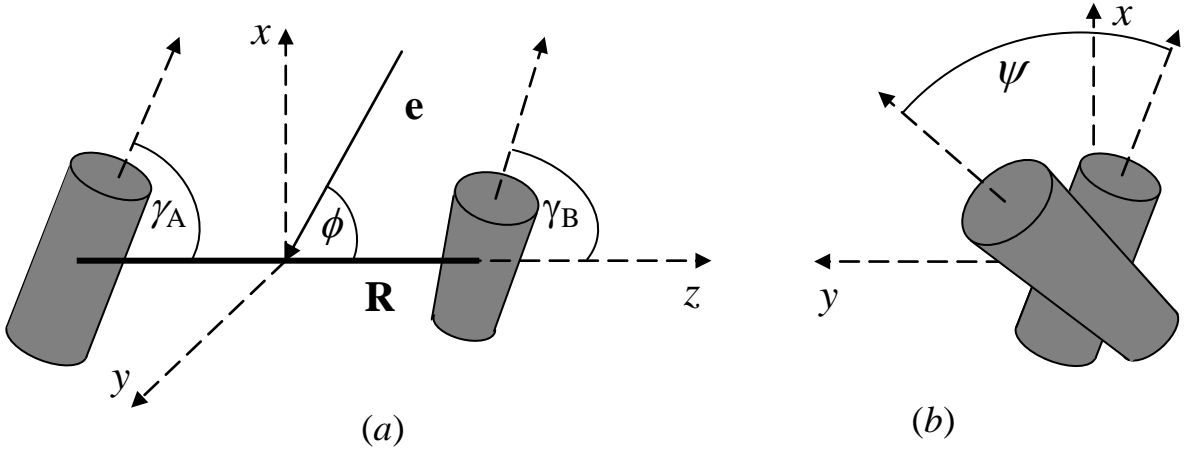


Figure 4: Geometry of the tumbling pair system, for a pair of cylindrical particles

As before, the polarization of the incoming and outgoing radiation is considered to be linear.

Representing the polarization in the laboratory frame, generally we have;

$$\mathbf{e}_i^{(\lambda)} = \sin \phi \cos \theta \hat{\mathbf{x}} + \sin \phi \sin \theta \hat{\mathbf{y}} + \cos \phi \hat{\mathbf{z}} \quad . \quad (2.14)$$

In the case of the tumbling cylindrical pair, the polarizability tensor of each particle is diagonal when expressed with respect to the corresponding particle's reference frame;

$$\boldsymbol{\alpha}^\xi = \begin{pmatrix} \alpha_\perp^\xi & 0 & 0 \\ 0 & \alpha_\perp^\xi & 0 \\ 0 & 0 & \alpha_\parallel^\xi \end{pmatrix} \quad (2.15)$$

However this frame rotates with the tumbling pair. It makes more sense to refer all vector and tensor components in the general energy expression (2.6) to a laboratory-fixed frame in which the polarization components are static, and to this end the polarizability for each particle must be recast in the laboratory-fixed frame. By appropriate unitary transformations, we find the following results for particles A and B :

$$\alpha^A \Big|_{\text{Fixed frame}} = \alpha_\parallel^A \begin{pmatrix} 1 - \eta^A \cos^2 \gamma_A & 0 & \eta^A \cos \gamma_A \sin \gamma_A \\ 0 & 1 - \eta^A & 0 \\ \eta^A \cos \gamma_A \sin \gamma_A & 0 & 1 - \eta^A \sin^2 \gamma_A \end{pmatrix} \quad (2.16.a)$$

and

$$\alpha_{ij}^B \Big|_{\text{Fixed frame}} = \alpha_\parallel^B \begin{pmatrix} (1 - \eta^B \cos^2 \gamma_B) \cos^2 \psi + (1 - \eta^B) \sin^2 \psi & \eta^B \sin^2 \gamma_B \cos \psi \sin \psi & \eta^B \cos \gamma_B \sin \gamma_B \cos \psi \\ \eta^B \sin^2 \gamma_B \sin \psi \cos \psi & (1 - \eta^B \cos^2 \gamma_B) \sin^2 \psi + (1 - \eta^B) \cos^2 \psi & \eta^B \cos \gamma_B \sin \gamma_B \cos \psi \\ \eta^B \cos \gamma_B \sin \gamma_B \cos \psi & \eta^B \cos \gamma_B \sin \gamma_B \sin \psi & (1 - \eta^B \sin^2 \gamma_B) \end{pmatrix}. \quad (2.16.b)$$

Here we have introduced the anisotropy factors $\eta^\xi \equiv (\alpha_\parallel^\xi - \alpha_\perp^\xi) / \alpha_\parallel^\xi$ to simplify the expressions. Given the complexity that ensues, we restrict consideration to that of an isotropic average with respect to the incoming light, the calculation of which requires the use of a phase-average method [37]. In this case the induced energy shift is given by,

$$\begin{aligned} \langle \Delta E_{ind} \rangle = & \frac{I}{\epsilon_0 c} \text{Re} \left[\left\{ \frac{1}{3} j_0(kR) - \frac{1}{6} j_2(kR) \right\} \left\{ V_{xx} (\alpha_{xx}^A \alpha_{xx}^B + \alpha_{yy}^A \alpha_{yy}^B + \alpha_{zx}^A \alpha_{zx}^B) + V_{zz} (\alpha_{xz}^A \alpha_{zx}^B + \alpha_{zz}^A \alpha_{zz}^B) \right\} \right. \\ & \left. + \frac{1}{2} j_2(kR) \left\{ V_{xx} \alpha_{zx}^A \alpha_{xz}^B + V_{zz} \alpha_{zz}^A \alpha_{zz}^B \right\} \right], \end{aligned} \quad (2.17)$$

where we have used $\alpha_{ij}^{\xi}|_{Fixed\ frame} \equiv \alpha_{ij}^{\xi}$ to simplify notation, with the explicit components for each particle determined by equation (2.16). The resulting expression can be explicitly calculated by using equation (2.8), giving;

$$\begin{aligned}
\langle \Delta E_{ind} \rangle &= \frac{I}{4\pi\epsilon_0^2 c R^3} \\
&\left[\left[\left(-kR + \frac{3}{kR} - \frac{1}{k^3 R^3} \right) \frac{1}{4} \sin 2kR - \left(1 - \frac{1}{k^2 R^2} \right) \frac{1}{2} \cos 2kR \right] \left(\alpha_{xx}^A \alpha_{xx}^B + \alpha_{yy}^A \alpha_{yy}^B \right) \right. \\
&+ \left[-\left(\frac{2}{kR} - \frac{1}{k^3 R^3} \right) \frac{1}{2} \sin 2kR + \left(1 - \frac{1}{k^2 R^2} \right) \cos 2kR + \sin^2 kR \right] \alpha_{zx}^A \alpha_{zx}^B \\
&+ \left[-\left(\frac{2}{kR} - \frac{1}{k^3 R^3} \right) \frac{1}{2} \sin 2kR + \left(1 - \frac{1}{k^2 R^2} \right) \cos 2kR - \cos^2 kR \right] \alpha_{xz}^A \alpha_{xz}^B \\
&+ \left[\left(\frac{1}{kR} - \frac{1}{k^3 R^3} \right) \sin 2kR + \frac{2}{k^2 R^2} \cos 2kR \right] \alpha_{zz}^A \alpha_{zz}^B \left. \right]
\end{aligned} \tag{2.18}$$

The corresponding laser-induced force, directly deducible from this expression, is explicitly given in the original papers [19,21].

2.4 Collinear pair

In this case we consider two cylindrically symmetric particles aligned collinearly, i.e., their principal axes of symmetry coincide, serving to define the axis z as shown in Fig. 5; owing to

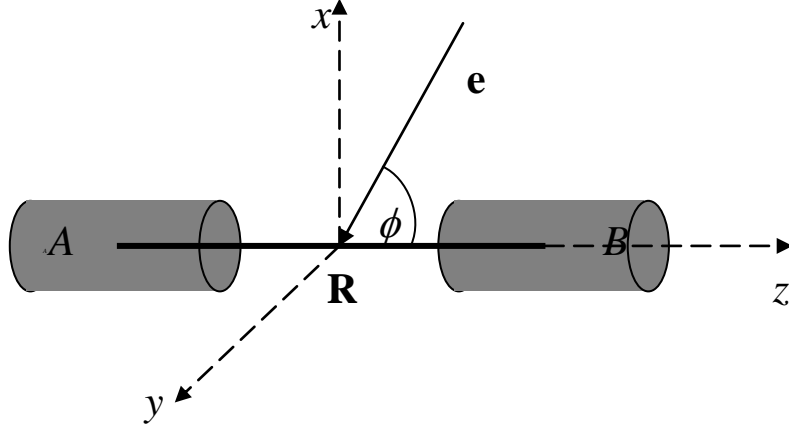


Figure 5: Geometry for a pair of collinear and cylindrical symmetric particles

the symmetry of the system it is readily seen that the induced energy shift is independent of the angle θ shown in Fig. 3. Therefore the polarization vector now takes the simpler form;

$$\mathbf{e} = \sin \phi \hat{\mathbf{x}} + \cos \phi \hat{\mathbf{z}}. \quad (2.19)$$

In this case we have that the polarisability tensor for each particle is given by

$$\alpha_{ij}^{(\xi)} = \begin{pmatrix} \alpha_{\perp}^{(\xi)} & 0 & 0 \\ 0 & \alpha_{\perp}^{(\xi)} & 0 \\ 0 & 0 & \alpha_{\parallel}^{(\xi)} \end{pmatrix}, \quad (2.20)$$

where we chose the molecular frame to coincide with that of the particles ($(x, y, z) \equiv (x_A, y_A, z_A) \equiv (x_B, y_B, z_B)$). From equations (2.19) and (2.20), the induced energy shift can be expressed as;

$$\Delta E_{ind}(k, \mathbf{R}) = \left(\frac{I}{2\pi\epsilon_0^2 c R^3} \right) \left\{ \left[\alpha_{\perp}^A \alpha_{\perp}^B \sin^2 \phi - 2\alpha_{\parallel}^A \alpha_{\parallel}^B \cos^2 \phi \right] \left[\cos(kR) + kR \sin(kR) \right] \right. \\ \left. - \alpha_{\perp}^A \alpha_{\perp}^B \sin^2 \phi k^2 R^2 \cos(kR) \right\} \cos(\mathbf{k} \cdot \mathbf{R}), \quad (2.21)$$

and the induced force as;

$$\begin{aligned}
\mathbf{F}_{ind} &= -\frac{\partial \Delta E_{ind}}{\partial \mathbf{R}} = -\frac{\partial \Delta E_{ind}}{\partial R} \hat{\mathbf{z}} \\
&= \left(\frac{I}{2\pi\epsilon_0^2 c R^4} \right) \times \left\{ \left(\alpha_{\perp}^A \alpha_{\perp}^B \sin^2 \phi - 2\alpha_{\parallel}^A \alpha_{\parallel}^B \cos^2 \phi \right) \times \right. \\
&\quad \left[\left(3 \cos kR + 3kR \sin kR - k^2 R^2 \sin kR \right) \cos(\mathbf{k} \cdot \mathbf{R}) + \left(k_z R \cos kR + k_z k R^2 \sin kR \right) \sin(\mathbf{k} \cdot \mathbf{R}) \right] \\
&\quad \left. - \alpha_{\perp}^A \alpha_{\perp}^B \sin^2 \phi \left[\left(k^2 R^2 \cos kR + k^3 R^3 \sin kR \right) \cos(\mathbf{k} \cdot \mathbf{R}) + k_z k^2 R^3 \cos kR \sin(\mathbf{k} \cdot \mathbf{R}) \right] \right\}.
\end{aligned} \tag{2.22}$$

If the particles have spherical symmetry, then $\alpha_{\perp}^{\xi} = \alpha_{\parallel}^{\xi} = \alpha_0^{\xi}$, and the induced energy shift and the induced force are more simply expressible as;

$$\begin{aligned}
\Delta E_{ind}^{symm}(k, \mathbf{R}) &= \left(\frac{I}{2\pi\epsilon_0^2 c R^3} \right) \alpha_0^A \alpha_0^B \times \\
&\quad \left\{ \left[\sin^2 \phi - 2 \cos^2 \phi \right] \left[\cos(kR) + kR \sin(kR) \right] - \sin^2 \phi k^2 R^2 \cos(kR) \right\} \cos(\mathbf{k} \cdot \mathbf{R}),
\end{aligned} \tag{2.23.a}$$

$$\begin{aligned}
\mathbf{F}_{ind}^{symm} &= \left(\frac{I}{2\pi\epsilon_0^2 c R^4} \right) \alpha_0^A \alpha_0^B \left\{ \left(\sin^2 \phi - 2 \cos^2 \phi \right) \times \right. \\
&\quad \left[\left(3 \cos kR + 3kR \sin kR - k^2 R^2 \sin kR \right) \cos(\mathbf{k} \cdot \mathbf{R}) + \left(k_z R \cos kR + k_z k R^2 \sin kR \right) \sin(\mathbf{k} \cdot \mathbf{R}) \right] \\
&\quad \left. - \sin^2 \phi \left[\left(k^2 R^2 \cos kR + k^3 R^3 \sin kR \right) \cos(\mathbf{k} \cdot \mathbf{R}) + k_z k^2 R^3 \cos kR \sin(\mathbf{k} \cdot \mathbf{R}) \right] \right\}.
\end{aligned} \tag{2.23.b}$$

In this case it is interesting to demonstrate the considerable simplification that can be effected if we consider $kR \ll 1$, and therefore $\cos(\mathbf{k} \cdot \mathbf{R}) \approx 1$, $\cos kR \approx 1$, and $\sin kR \approx kR$. Then the above expressions reduce to;

$$\Delta E_{ind}^0(k, \mathbf{R}) = \left(\frac{I}{2\pi\epsilon_0^2 c R^3} \right) \left[\alpha_{\perp}^A \alpha_{\perp}^B \sin^2 \phi - 2\alpha_{\parallel}^A \alpha_{\parallel}^B \cos^2 \phi \right], \tag{2.24.a}$$

$$\mathbf{F}_{ind}^0 = \left(\frac{3I}{2\pi\epsilon_o^2 cR^4} \right) (\alpha_{\perp}^A \alpha_{\perp}^B \sin^2 \phi - 2\alpha_{\parallel}^A \alpha_{\parallel}^B \cos^2 \phi) , \quad (2.24.b)$$

which in turn become even more compact for the spherically symmetric case;

$$\Delta E_{ind}^{0,symm} = \frac{I}{2\pi\epsilon_o^2 cR^3} \alpha_0^A \alpha_0^B (3 \sin^2 \phi - 2) \quad (2.25.a)$$

$$\mathbf{F}_{ind}^{0,symm} = \frac{3I}{2\pi\epsilon_o^2 cR^4} \alpha_0^A \alpha_0^B (3 \sin^2 \phi - 2) \quad (2.25.b)$$

Finally, consider a pair that can freely tumble, whilst retaining a fixed collinear orientation of its component particles. Then by averaging over all possible directions for the radiation we have;

$$\langle \Delta E_{ind} \rangle = \frac{I}{3\pi\epsilon_o^2 cR^3} \left\{ [\alpha_{\perp}^A \alpha_{\perp}^B - \alpha_{\parallel}^A \alpha_{\parallel}^B] [\cos(kR) + kR \sin(kR)] - \alpha_{\perp}^A \alpha_{\perp}^B k^2 R^2 \cos(kR) \right\} \cos(\mathbf{k} \cdot \mathbf{R}) \quad (2.26)$$

and in the short range;

$$\langle \Delta E_{ind}^0 \rangle = \left(\frac{I}{3\pi\epsilon_o^2 cR^3} \right) \times [\alpha_{\perp}^A \alpha_{\perp}^B - \alpha_{\parallel}^A \alpha_{\parallel}^B] . \quad (2.27)$$

The laser-induced force can be calculated in a similar manner. Clearly, in the spherical case, $\alpha_{\perp}^{\xi} = \alpha_{\parallel}^{\xi}$, giving vanishing results for both the energy shift and force. However, this short-range asymptote is not representative of the complex patterning of energy and force observed at longer distances. The behavior beyond the short-range is itself of considerable interest, and it is a subject we explore in due detail in Sect. 2.6.

2.5 Cylindrical parallel pair

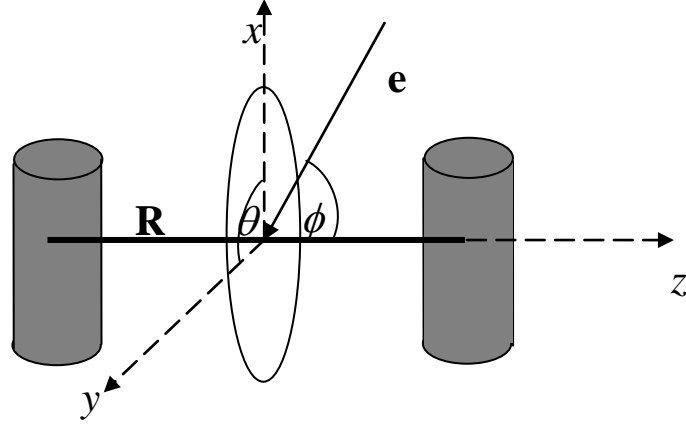


Figure 6: Geometry for a pair of parallel and cylindrical symmetric particles

Another interesting case is where the two cylindrically-symmetric particles are parallel to each other, and perpendicular to their relative displacement vector \mathbf{R} – see Fig. 6. In this case, given the geometry of the system, it is necessary to retain both angular degrees of freedom, ϕ and θ in equation (2.14). The polarizability for this system is given by;

$$\alpha_{ij}^{(\xi)} = \begin{pmatrix} \alpha_{\parallel}^{(\xi)} & 0 & 0 \\ 0 & \alpha_{\perp}^{(\xi)} & 0 \\ 0 & 0 & \alpha_{\perp}^{(\xi)} \end{pmatrix}. \quad (2.28)$$

Note the difference from the previous case, equation (2.20), due to the effective rotation of the particles in the xz -plane (from the definition of the molecular angles in the tumbling pair section, we can see that in this case the polarizability can be obtain from expressions (2.16a) and (2.16b) for $\gamma_A = \gamma_B = \pi/2$, $\psi = 0$). The induced energy shift $\Delta E_{ind}(k, \mathbf{R})$ is now given by;

$$\begin{aligned} \Delta E_{ind}(k, \mathbf{R}) = & \\ & \left(\frac{I}{2\pi\epsilon_0^2 c R^3} \right) \left\{ \left[\alpha_{\parallel}^A \alpha_{\parallel}^B \sin^2 \phi \cos^2 \theta + \alpha_{\perp}^A \alpha_{\perp}^B \sin^2 \phi \sin^2 \theta - 2\alpha_{\perp}^A \alpha_{\perp}^B \cos^2 \phi \right] \left[\cos(kR) + kR \sin(kR) \right] \right. \\ & \left. - \left[\alpha_{\parallel}^A \alpha_{\parallel}^B \sin^2 \phi \cos^2 \theta + \alpha_{\perp}^A \alpha_{\perp}^B \sin^2 \phi \sin^2 \theta \right] k^2 R^2 \cos(kR) \right\} \cos(\mathbf{k} \cdot \mathbf{R}) \end{aligned} \quad (2.29)$$

and the induced force is;

$$\begin{aligned}
\mathbf{F}_{ind} &= -\frac{\partial \Delta E_{ind}}{\partial \mathbf{R}} \\
&= \left(\frac{I}{2\pi\epsilon_o^2 c R^3} \right) \left\{ \left\{ \left[\alpha_{\parallel}^A \alpha_{\parallel}^B \sin^2 \phi \cos^2 \theta + \alpha_{\perp}^A \alpha_{\perp}^B \sin^2 \phi \sin^2 \theta - 2\alpha_{\perp}^A \alpha_{\perp}^B \cos^2 \phi \right] \left[3 \cos(kR) + 3kR \sin(kR) - k^2 R^2 \cos(kR) \right] \right. \right. \\
&\quad \left. \left. - \left[\alpha_{\parallel}^A \alpha_{\parallel}^B \sin^2 \phi \cos^2 \theta + \alpha_{\perp}^A \alpha_{\perp}^B \sin^2 \phi \sin^2 \theta \right] \left[k^2 R^2 \cos(kR) + k^3 R^3 \sin(kR) \right] \right\} \cos(\mathbf{k} \cdot \mathbf{R}) \right. \\
&\quad \left. + \left\{ \left[\alpha_{\parallel}^A \alpha_{\parallel}^B \sin^2 \phi \cos^2 \theta + \alpha_{\perp}^A \alpha_{\perp}^B \sin^2 \phi \sin^2 \theta - 2\alpha_{\perp}^A \alpha_{\perp}^B \cos^2 \phi \right] \left[k_z R \cos(kR) + k_z k R^2 \sin(kR) \right] \right. \right. \\
&\quad \left. \left. - \left[\alpha_{\parallel}^A \alpha_{\parallel}^B \sin^2 \phi \cos^2 \theta + \alpha_{\perp}^A \alpha_{\perp}^B \sin^2 \phi \sin^2 \theta \right] \left[k_z k^2 R^3 \cos(kR) \right] \right\} \sin(\mathbf{k} \cdot \mathbf{R}) \right\}. \tag{2.30}
\end{aligned}$$

In the short range approximation ($kR \ll 1$) the corresponding expressions are;

$$\Delta E_{ind}^0 = \frac{I}{2\pi\epsilon_o^2 c R^3} \left\{ \left[\alpha_{\parallel}^A \alpha_{\parallel}^B \cos^2 \theta + \alpha_{\perp}^A \alpha_{\perp}^B \sin^2 \theta \right] \sin^2 \phi - 2\alpha_{\perp}^A \alpha_{\perp}^B \cos^2 \phi \right\} \tag{2.31.a}$$

$$F_{z, ind}^0 = \left(\frac{3I}{2\pi\epsilon_o^2 c R^4} \right) \left[\alpha_{\perp}^A \alpha_{\perp}^B \left(\sin^2 \phi (2 + \sin^2 \theta) - 2 \right) + \alpha_{\parallel}^A \alpha_{\parallel}^B \sin^2 \phi \cos^2 \theta \right]. \tag{2.31.b}$$

Again, if the parallel pair freely tumbles with respect to the electromagnetic field, it is necessary to consider the isotropic average case, and we can see from equation (2.27) that

$$\langle \Delta E_{ind}^0 \rangle = \frac{I}{6\pi\epsilon_o^2 c R^3} \left[\alpha_{\parallel}^A \alpha_{\parallel}^B - \alpha_{\perp}^A \alpha_{\perp}^B \right] \tag{2.32}$$

$$\langle F_{z, ind}^0 \rangle = \left(\frac{I}{2\pi\epsilon_o^2 c R^4} \right) \times \left[\alpha_{\parallel}^A \alpha_{\parallel}^B - \alpha_{\perp}^A \alpha_{\perp}^B \right]. \tag{2.33}$$

In a case where the particles have spherical symmetry, it is readily verified that the above results reduce to the same limiting expressions as those given in previous sections.

The above results, for cylindrical particles in various configurations, have been applied to single-walled carbon nanotubes. These particles are of interest not only for their intrinsic properties and applications; since they are strongly polarizable species, they also afford ideal opportunities to exploit the quadratic dependence on polarizability featured in the force

equations. Assuming that the α_{\perp} and α_{\parallel} values are consistent with the corresponding static polarizabilities, then for nanotubes 200 nm in length and 0.4 nm in radius, separated by a distance $R = 2$ nm, and with an incident intensity $I = 1 \times 10^{16}$ W m⁻², the results deliver forces ranging between 10^{-12} and 10^{-5} N, according to the geometry [21]. Significantly, this full range of values is amenable to determination by atomic force microscopy. However, there may be a more important consequence: the wide variation in values, and the scale of the highest values, suggests that there is a realistic possibility for the nanomanipulation of carbon nanotubes, based on laser control of the optomechanical forces.

2.6 Spherical particles

For spherical particles, the energy shift may be obtained by setting $\alpha_o^{\xi} = \alpha_{\parallel}^{\xi} = \alpha_{\perp}^{\xi}$ in equations (2.21) or (2.29). This shift may be expressed as a function of the geometric parameters illustrated in Fig. 7 as follows;

$$\Delta E(\mathbf{k}, \mathbf{R}) = \left(\frac{2I}{\epsilon_0 c} \right) \text{Re} \left\{ \alpha_0^A V_{xx}(k, \mathbf{R}) \alpha_0^B \right\} \cos(kR \sin \phi \cos \zeta), \quad (2.34)$$

Contour plots can be obtained of the energy surface determined by equation (2.34), giving detailed information about the location of the system's stability points – see Fig. 8. A host of interesting features emerge even from the examples exhibited here [38, 39]. In each energy landscape, local minima distinguish optical binding configurations. The contours intersect the abscissa scale orthogonally, reflecting an even dependence on each angular variable; the variation in the domain ($0 \leq \phi \leq \pi/2$, $0 \leq \zeta \leq \pi/2$) is notionally revealed by unfolding along the distance axis. The physical significance is that a system whose (kR, ζ, ϕ) configuration has $\phi = 0$ or $\zeta = 0$, but not situated at a local minimum, is always subject to a force drawing it towards a neighboring minimum without change of orientation. For the same reason, there is no torque when $\phi = \pi/2$ or $\zeta = \pi/2$. However a system in an arbitrary configuration will generally be subject to forces leading to both forces and torques. For example, inspection of Fig. 8(a) shows that whilst a pair in the configuration $(6.0, \pi/4, 0)$ is subject to a torque tending to increase ϕ to $\pi/2$, its trajectory will be accompanied by forces that tend to first increase and then decrease R . The details, which will additionally involve changes in ζ , can of course be determined from the total derivative of (2.34). Other features, also exemplified in Fig. 8(a), are off-axis islands of stability such as the one that can be identified at $(10, \pi/10, 0)$. In

general the optically induced pair potential provides a prototypical template for the optical assembly of larger numbers of particles, facilitating the optical fabrication of structures of molecules, nanoparticles, microparticles, and colloidal particles.

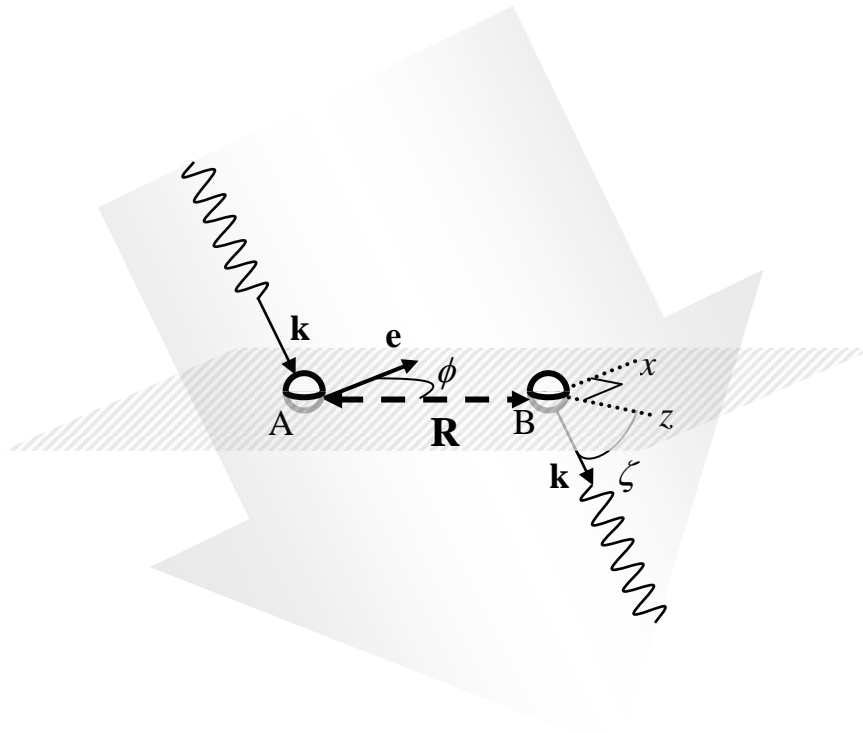


Figure 7: Particles A and B, displaced by \mathbf{R} , trapped in a polarised laser beam. The polarization vector, \mathbf{e} , defines the x -axis, forming an angle ϕ with \mathbf{R} . Together, these vectors define the x,z -plane, the beam propagation vector \mathbf{k} subtending an angle ζ on to z .

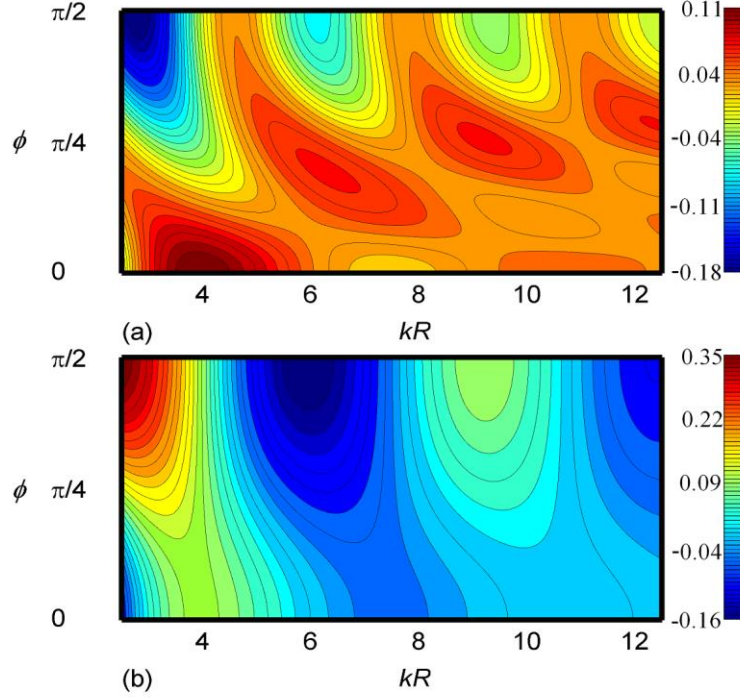


Figure 8: Contour maps of optically induced pair energy. Plots of ΔE as a function of ϕ and kR : (a) $\zeta = 0$; (b) $\zeta = \pi/2$. The variation of ΔE with kR along the abscissa, $\phi = 0$, shows its first two maxima at $kR \sim 4.0, 10.5$, the first (non-proximal) minimum, at $kR \sim 7.5$ (compare Fig. 1). The horizontal scale typically spans distances R of several hundred nanometers, depending on the value of k (see text). The units of the color scale are $\alpha_o^{(A)} \alpha_o^{(B)} 2Ik^3 / (4\pi\epsilon_o^2 c)$. Adapted from refs [38, 39].

2.7 Spherical particles in a Laguerre-Gaussian beam

The nature and form of optically induced forces between particles in an optical vortex are of special interest. Here, we entertain the possibilities afforded by having two or more particles (for simplicity assumed to be spherical) trapped in a Laguerre-Gaussian (LG) beam – or two such beams, counterpropagating to offset Maxwell-Bartoli forces. First, consider particles A and B trapped in the annular high-intensity region of an LG beam with arbitrary l and $p = 0$, i.e. an optical vortex with one radial node at the beam centre. For significant forces to arise, the inter-particle distance R will usually be small compared to the radius of the optical trap, and it is helpful to recast the energy and force equations in terms of the angular displacement $\Delta\psi$ between A and B ; see Fig. 9 (a). The general result (for arbitrary p) is as follows;

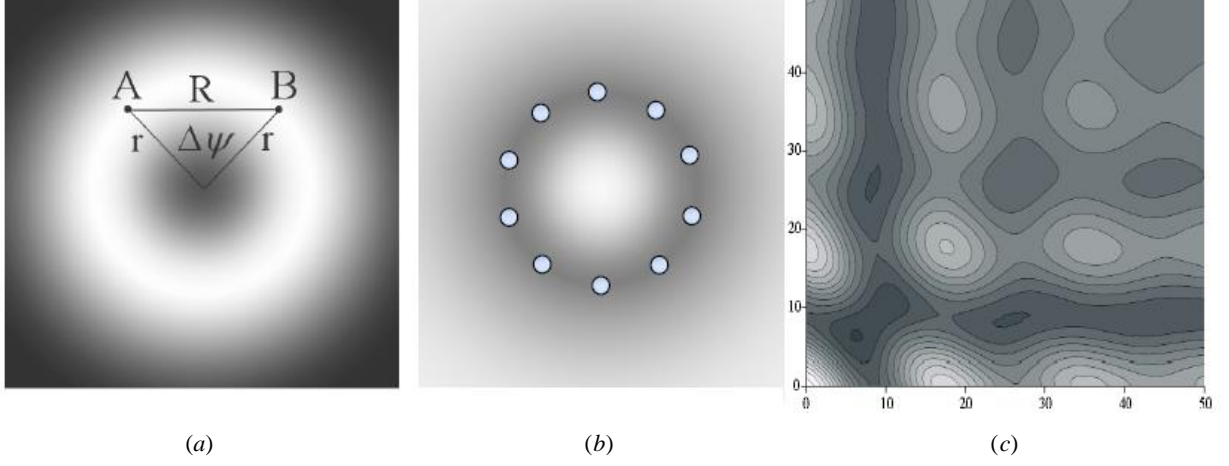


Figure 9: (a) Geometry of a particle pair in a Laguerre-Gaussian beam ($p = 0$); (b) Clustering of nanoparticles in an LG beam; (c) Contour graphs of ΔE_{ABC}^0 against $\Delta\psi_1$ (x-axis) and $\Delta\psi_2$ (y-axis) for three particles in an LG beam with $l = 20$; lighter shading denotes higher values of ΔE_{ABC}^0 . Adapted from refs [22, 40, 41]

$$\Delta E_{ind} = \left(\frac{I f_{lp}^2 \alpha_0^2}{4\pi\epsilon_0^2 c A_{lp} R^3} \right) \left\{ \cos^2 \phi (\cos kR + kR \sin kR - k^2 R^2 \cos kR) - 2 \sin^2 \phi (\cos kR + kR \sin kR) \right\} \cos(l \Delta\psi). \quad (2.35)$$

where f_{lp} and A_{lp} are standard LG beam functions as defined in chapter 1, and usually α_0 is the polarisability of a spherical nanoparticle (the same for A and B), $\hbar ck$ denotes the input photon energy, ϕ is again the angle between the polarization of the input radiation and \mathbf{R} , and $\Delta\psi = \psi_B - \psi_A$ is the azimuthal displacement angle. In the short-range region ($kR \ll 1$), the leading term of equation (1) is determined from Taylor series expansions of $\sin(kR)$ and $\cos(kR)$. By the use simple trigonometry, the result ΔE_{ind} can be expressed as [22, 40, 41];

$$\Delta E_{ind}^0 = \left[\frac{I f_{lp}^2 \alpha_0^2 (1 - 3 \sin^2 \phi)}{8\sqrt{2}\pi\epsilon_0^2 r^3 c A_{lp}} \right] \frac{\cos(l \Delta\psi)}{(\eta - \cos \Delta\psi)^{3/2}}. \quad (2.36)$$

Here, η is a damping factor whose introduction, in place of the unity that emerges from simple trigonometry precludes a singularity at $\Delta\psi = 0$.

The result has a number of interesting features: (i) at $l = 0$ – i.e. for a conventional Gaussian laser beam – a single energy minimum occurs at $\Delta\psi = 180^\circ$, illustrating that the energetically most favorable position of the particles in the beam cross-section is where they are diametrically opposite each other, as might be expected; (ii) for odd values of $l > 1$, only a local minimum (not the energetically most favorable) arises for this configuration; (iii) for even values of l , a local *maximum* occurs at 180° ; (iv) generally, for $l \neq 0$, there are l angular minima and $(l - 1)$ maxima. Additional features reflect the behavior associated with increasing values of l : (v) the number of positions for which the particle pair can be mutually trapped increases, becoming less energetically favorable as the angular disposition increases towards diametric opposition, and; (vi) absolute minima are found at decreasing values of $\Delta\psi$ physically signifying a progression towards particle clustering.

To identify the possibilities for stable formations of more than two particles, as illustrated in Fig. 9 (b), the two-particle analysis is readily extended to a system of three (or more) particles. In this case ΔE_{ABC}^0 is determined by summing the pairwise laser-induced interactions of the three particles with each other, employing variables $\Delta\psi_1$ and $\Delta\psi_2$ as the azimuthal displacements between particles *A-B* and *B-C* respectively. A typical contour plot of ΔE_{ABC}^0 against $\Delta\psi_1$ and $\Delta\psi_2$ is exhibited in Fig. 9 (c). Such results are indicative of a rich scope for further theoretical and experimental exploration.

3 Overview of applications

The body of experimental work on optical binding, and related studies, is growing apace. We here summarize just a fragment of the novel work being done by a number of different research groups working in this area. Most experimental research has been stimulated by an interest in applying optical binding to the organization and manipulation of matter at scales comparable to the wavelength of light. In such a context, it has to be borne in mind that optical binding forces will have a profound effect, modifying the outcome of all optical manipulation techniques where more than one particle is involved [42]. Obvious examples are processes involving the assembly of optical structures using holographic optical traps [43]; equally, the two-dimensional assembly of particles in the presence of counterpropagating beams results from the combined effects of optical trapping and binding

[44]. Although the systems used and the setup designs vary significantly, these and other such studies have common goals – principally to understand the nature of the binding forces due to the presence of an electromagnetic field, and to develop tools for the non-contact control of matter on the micron- and sub-micron/nano-scale.

One of the most common systems used to demonstrate optical binding comprises micron-sized essentially spherical polyethylene beads in a liquid suspension. In two of the first reports by Burns *et al.* [2,4], it was noted that the relative position of a pair of such spheres were influenced by each other when placed in an optical trap. When the spheres were well separated in the trap their motions along the trap appeared random, but as they approached each other they appeared to depart from diffusive behavior, tending to spend more time in relatively close proximity. The relative motion of the pair was recorded by studying the diffraction patterns thereby created in the scattered field. Significantly, it was shown that there are discrete separations at which the particles are more likely to be found, and that the positions of the inferred neighboring energy minima differ by distances approximately equal to the wavelength of the light.

In later work [45,46], it was demonstrated that optical binding forces are at least partly responsible for the self-arrangement of optically trapped particles separated by distances ranging up to a few wavelengths. Several different cases have been reported, as illustrated in Fig. 10, and it has been shown that the binding force can dominate over the usual (optical tweezer) gradient trapping force in systems where one expects a large number of particles to arrange according to a trapping template. When a free particle approaches an already formed structure, being subject to a potential energy landscape already patterned by many-body optical interference, the added sphere becomes accommodated within the whole ensemble – which then re-organizes until it reaches a new minimum energy configuration. It is important to emphasize that it is extremely difficult to disentangle optical forces due to gradient and scattering forces in most of these experiments, and that the generation of ‘optical crystals’ as shown in these examples is generally due to contributions from both types of interaction, as is specifically shown in Figure 11.

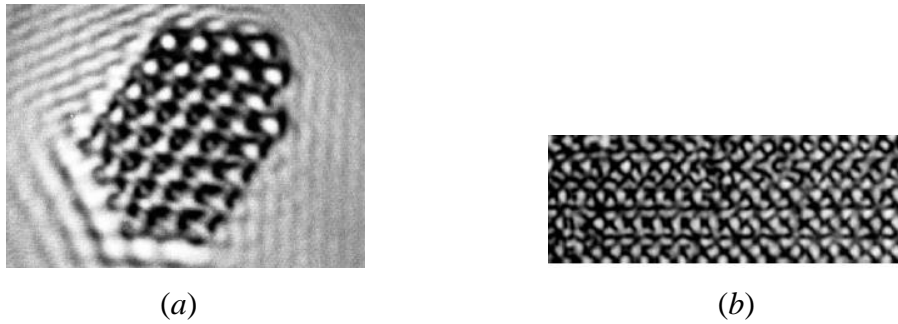


Figure 10: (a) Self-assembled 2D ‘optical crystal’ formed in a $30\mu\text{m}$ Gaussian trap generated by a single laser beam. The multiple coherent scattering of the polystyrene spheres ($3\mu\text{m}$) generates sinusoidal fringes through its interference with the trap. Adapted from [45]; (b) 1D optical crystals formed in fringes created by interference of two plane waves, $3\mu\text{m}$ polystyrene beads self-organize along each trap, optical binding forces promoting a regular, equidistant placement. Adapted from [46].

It is worth noting that the experimental setup used in the studies whose results are exemplified above is commonly referred to as ‘transverse optical binding’ [47], meaning that the wave-vector of the electromagnetic field is perpendicular to the plane containing the 2D optical crystal, or the axis of a 1D optical chain. As illustrated in Fig. 11, this setup takes advantage of a container cell to confine the optical crystal. Nonetheless such a configuration admits numerous possibilities of scattering from the cell, making it difficult to analyze the optical binding contribution. A different approach is to achieve ‘longitudinal optical binding’ [48-51], Fig. 12, where two counterpropagating (non-coherent) beams impinge on the system.

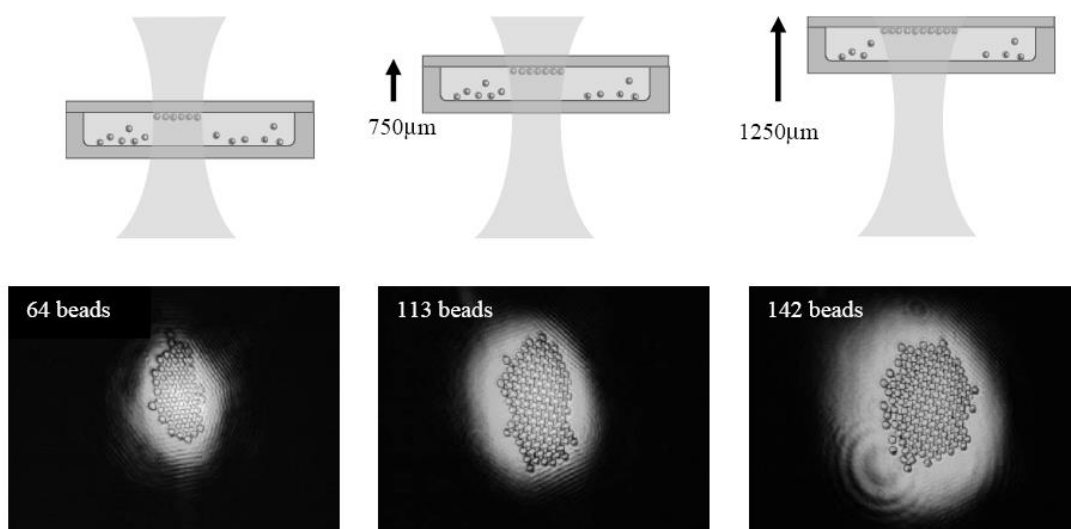


Figure 11: 2D optical crystals resulting from the combination of binding and trapping in a Gaussian trap produced by 1 Watt laser power at 532 nm. Adapted from [46]

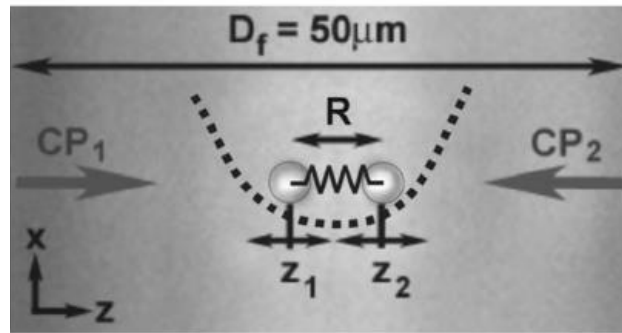


Figure 12: Counterpropagating light fields (CP1 and CP2: 1070 nm) are delivered by optical fibers with a separation D_f . A pair array forms in the gap between the two fibers; R is the equilibrium separation of the sphere centers and z_1, z_2 indicate small displacements from equilibrium along the axis. The array center of symmetry coincides with half the fiber separation. The two normal modes of the bound pair are indicated: the dashed line represents the potential related to the center of mass motion of the two-sphere system; the zig-zag between the two spheres indicates the optically induced pair potential, determining relative motion within the system. Adapted from [51].

Completing the picture, there have also been studies of optical binding between nano-metallic particles trapped in electromagnetic fields [52-55]. Indeed the detection of light-induced aggregation in 10 nm gold clusters was first reported over ten years ago [52]. At the time, this was attributed to van der Waals-like forces between closely approaching clusters and cluster aggregates. A subsequent theoretical study [53] showed that the inter-particle interaction energy is a sensitive function of the particle size. More recent theoretical work has shown that such optical binding forces are significantly stronger than traditional van der Waals forces, and that there are realistic possibilities to exploit optically induced forces for the non-contact organization of novel metallic structures [54] such as the metallic necklaces reported in [55].

4 Discussion

Relating theory to experiment in this field is perhaps more than usually difficult, but it is a challenge that carries a promise of rich rewards, in the form of new techniques for the nanomanipulation of matter. Part of the problem is that producing suitable conditions for the sought effects generally necessitates the use of specialized cells or optical traps, each of which can generate additional, partly contributory optical effects – which can then compete with optical binding in most cases. Another difficulty is that many existing descriptions of optical binding mechanism are a little vague, and it is not always clear whether two different descriptions amount to the same, or to potentially competing phenomena. In the hope of bringing more clarity and precision to the field, the theoretical methods and results we have presented in this chapter are based on a robust and thorough quantum electrodynamical analysis of optically induced inter-particle interactions. In this framework it is understood that laser-induced forces and torques between nanoparticles occur by pairwise processes of stimulated photon scattering. The analysis clarifies the fundamental involvement of quantum interactions with the throughput radiation, and also the form of electromagnetic coupling between particles. It further reveals that additional torque features arise in an optical vortex.

In applying the results to nanoparticles (such as polystyrene beads) whose electronic properties are neither those of one large molecule, nor those of a chromophore aggregate, the molecular properties that appear in the given equations have to be translated into bulk quantities; the polarizability becomes the linear susceptibility, for example. Moreover, account has to be taken of the optical properties of the medium supporting the particles. In most of the experiments discussed in Section 3, it has been shown that the relative values of the refractive index between the beads and the surrounding medium significantly influence the optical binding phenomena, modifying the bead positions of stability. In fact, proper registration by the theory of the responsible local field effects is also straightforward; it is already known how the retarded potential of equation (2.7) is affected [56]. Alongside the incorporation of Lorentz field factors, the dependence on kR changes to a dependence on $n(\mathbf{c}k)kR$, where the multiplier is the complex refractive index. For example in a liquid illuminated by 800 nm radiation, when the refractive index at that wavelength is 1.40, the potential energy minimum registered in Fig. 1 at $kR \sim 7.5$ signifies a pair separation of 670 nm rather than 960 nm.

Recently, there has been fresh interest in the angular properties of the force fields resulting from optical binding. Multi-dimensional potential energy surfaces have been derived and shown to exhibit unexpected turning points, producing intricate patterns of local force and torque. Numerous local potential minimum and maximum can be identified, and islands of stability conducive to the formation of rings have been identified [38, 39]. The major challenge now to be addressed is to account for the effects of particle numbers, namely the additional and distinctive features that must arise when more than two isolated particles are involved. There are three distinct aspects to this. First and simplest, there is a need to identify those effects which will very obviously arise as a consequence of the superposition of optically modified pair potentials. Secondly, a full analysis needs to be made of the contributions from *multi*-particle processes of stimulated scattering, involving the entangled near-field interactions of more than two particles. And finally, since stimulated scattering releases throughput radiation essentially unchanged, *multiple processes* of stimulated scattering have to be entertained in order to properly address the kind of 1D arrays and 2D optical crystal structures that experiments have so beautifully revealed. We are confident that these challenges for the future will soon bear the fruit of establishing still better and clearer links between theory and experiment.

5 Acknowledgment

We are pleased to acknowledge that all of the QED work at UEA has been made possible through funding from the EPSRC. We also gratefully acknowledge many useful discussions of the work, especially with David Bradshaw and Justo Rodríguez at UEA, and Kishan Dholakia at the University of St. Andrews.

6 References

- [1] T. Thirunamachandran, *Mol. Phys.* 40, 393 (1980).
- [2] M. M. Burns, J.-M. Fournier and J. A. Golovchenko, *Phys. Rev. Letts.* 63, 1233 (1989).
- [3] G. Whitesides, *Angew. Chem. Int. Ed. Engl.* 29, 1209 (1990).

- [4] M. M. Burns, J.-M. Fournier and J. A. Golovchenko, *Science*, 249, 749 (1990).
- [5] P. W. Milonni and M. L. Shih, *Phys. Rev. A* 45, 4241 (1992).
- [6] F. Depasse and J.-M. Vigoureux, *J. Phys. D: Appl. Phys.* 27, 914 (1994).
- [7] P. W. Milonni and A. Smith, *Phys. Rev. A* 53, 3484 (1996).
- [8] P. C. Chaumet and M. Nieto-Vesperinas, *Phys. Rev. B* 64, 035422 (2001).
- [9] M. Nieto-Vesperinas, P. C. Chaumet and A. Rahmani, *Phil. Trans. R. Soc. Lond. A* 362, 719 (2004).
- [10] S. K. Mohanty, J. T. Andrews and P. K. Gupta, *Opt. Express* 12, 2746 (2004).
- [11] D. McGloin, A. E. Carruthers, K. Dholakia and E. M. Wright, *Phys. Rev. E* 69, 021403 (2004).
- [12] D. H. J. O'Dell, S. Giovanazzi, G. Kurizki, and V. M. Akulin, *Phys. Rev. Letts.* 84, 5687 (2000).
- [13] F. Dimer de Oliveira and M. K. Olsen, *Opt. Commun.* 234, 235 (2004).
- [14] N. K. Metzger, E. M. Wright and K. Dholakia, *New J. Phys.* 8, 139 (2006).
- [15] V. Karásek, K. Dholakia and P. Zemánek, *Appl. Phys. B* 84, 149 (2006).
- [16] J. Ng and C. T. Chan, *Opt. Lett.* 31, 2583, (2006).
- [17] T. M. Grzegorzcyk, B. A. Kemp and J.A. Kong, *J. Opt. Soc. Amer. A*, 23, 2324 (2006).
- [18] T. M. Grzegorzcyk, B. A. Kemp and J.A. Kong, *Phys. Rev. Lett.*, 96, 113903 (2006).
- [19] D. S. Bradshaw and D. L. Andrews, *Phys. Rev. A* 72, 033816 (2005): corr., *Phys. Rev. A* 73, 039903 (2006).
- [20] A. Salam, *J. Chem. Phys.* 124, 014302 (2006).
- [21] D. L. Andrews and D. S. Bradshaw, *Opt. Letts.* 30, 783 (2005).
- [22] D. S. Bradshaw and D. L. Andrews, *Opt. Letts.* 30, 3039 (2005).
- [23] D. L. Andrews, R. G. Crisp and D.S. Bradshaw, *J. Phys. B: At. Mol. Opt. Phys.* 39, S637 (2006).
- [24] H. B. G. Casimir and D. Polder, *Phys. Rev.* 73, 360 (1948).
- [25] P. W. Milonni, *The Quantum Vacuum: An Introduction to Quantum Electrodynamics* (Academic, San Diego CA, 1994) p.54
- [26] D. L. Andrews and L. C. Dávila Romero, *Eur. J. Phys.* 22, 447 (2001).
- [27] E. A. Power, *Eur. J. Phys.* 22, 453 (2001).
- [28] G. Jordan Maclay, H. Fearn and P. W. Milonni, *Eur. J. Phys.* 22, 463 (2001).
- [29] B. W. Alligood and A. Salam, *Mol. Phys.* 105, 395 (2007).

- [30] F. Capasso, J. N. Munday, D. Iannuzzi and H. B. Chan, *IEEE J. Select. Topics Quantum Electron.* 13, 400 (2007).
- [31] A. Altland and B. Simons, *Condensed Matter Field Theory* (University Press College, Cambridge, 2006) p.29
- [32] E. A. Power and S. Zienau, *Phil. Trans. R. Soc. A* 251, 427 (1959).
- [33] R. G. Woolley, *Proc. R. Soc. A* 321, 557 (1971).
- [34] E. A. Power and T. Thirunamachandran, *Amer. J. Phys.* 46, 370 (1978).
- [35] R. G. Woolley, *Int. J. Quantum Chem.* 74, 531 (1999).
- [36] R. D. Jenkins, G. J. Daniels and D. L. Andrews, *J. Chem. Phys.* 120, 11442 (2004).
- [37] D. L. Andrews and M. J. Harlow, *Phys. Rev. A* 29, 2796 (1984).
- [38] J. Rodríguez, L. C. Dávila Romero and D. L. Andrews, *J. Nanophotonics* 1, 019503 (2007).
- [39] L. C. Dávila Romero, J. Rodríguez and D. L. Andrews, *Opt. Commun.* (in press, 2007).
- [40] D. S. Bradshaw and D. L. Andrews, in *SPIE Proceedings – Nanomanipulation with Light*, 5736, 87 (2005).
- [41] D. S. Bradshaw and D. L. Andrews, in *SPIE Proceedings – Nanomanipulation with Light II*, 6131, 61310G (2006).
- [42] D. G. Grier, *Nature* 424, 810 (2003)
- [43] D. G. Grier, S-H. Lee, Y. Roichman and Y. Roichman, in *SPIE Proceedings – Complex Light and Optical Forces*, 6483, 64830D (2007).
- [44] C. D. Mellor, T. A. Fennerty and C. D. Bain, *Opt. Express* 14, 10079 (2006).
- [45] J-M. Fournier, G. Boer, G. Delacrétaz, P. Jacquot, J. Rohmer and R. P. Salathé, *SPIE Proceedings – Optical Trapping and Optical Micromanipulation*, 5514, 309 (2004).
- [46] J-M. Fournier, J. Rohmer, G. Boer, P. Jacquot, R. Johann, S. Mias and R. P. Salathé, in *SPIE Proceedings – Optical Trapping and Optical Micromanipulation II*, 5930, 59300Y (2005).
- [47] M. Guillon, *Opt. Express*, 14, 3045 (2006).
- [48] M. Guillon, in *SPIE Proceedings – Optical Trapping and Optical Micromanipulation II*, 5930, 59301T, (2005).
- [49] W. Singer, M. Frick, S. Bernet, and M. Ritsch-Marte, *J. Opt. Soc. Am. B*, 20, 1568 (2003).

- [50] N. K. Metzger, E. M. Wright, W. Sibbett and K. Dholakia, *Opt. Express*, 14, 3677 (2006).
- [51] N. K. Metzger, R. F. Marchington, M. Mazilu, R. L. Smith, K. Dholakia and E. M. Wright, *Phys. Rev. Lett.*, 98, 068102 (2007).
- [52] H. Ecksteing and U. Kreibig, *Z. Phys D.*, 26, 239 (1993).
- [53] K. Kimura, *J. Phys. Chem.*, 98, 11997 (1994).
- [54] A. J. Hallock, P. L. Redmond and L. E. Brus, *F PNAS*, 102, 1280 (2005).
- [55] G. Ramakrishna, Q. Dai, J. Zou, Q. Huo and Th. Goodson III, *J. Am. Chem. Soc.*, 129, 1848 (2007).
- [56] G. Juzeliūnas and D. L. Andrews, *Adv. Chem. Phys.* 112, 357 (2000).